ACS OMEGA

http://pubs.acs.org/journal/acsodf

Article

Signature of Oxide-Ion Conduction in Alkaline-Earth-Metal-Doped Y_3GaO_6

Pragati Singh, Raghvendra Pandey,* Tadeusz Miruszewski, Kacper Dzierzgowski, Aleksandra Mielewczyk-Gryn, and Prabhakar Singh*

Cite This: *ACS Omega* 2020, 5, 30395−30404

Read Online

ACCESS | Metrics & More | Article Recommendations | Supporting Information

ABSTRACT: We have studied alkaline-earth-metal-doped Y_3GaO_6 as a new family of oxide-ion conductor. Solid solutions of Y_3GaO_6 and 2% $-Ca^{2+}$-, $-Sr^{2+}$-, and $-Ba^{2+}$-doped Y_3GaO_6, i.e., $Y_{(3-0.06)}M_{0.06}GaO_{6-\delta}$ (M = Ca^{2+}, Sr^{2+}, and Ba^{2+}), were prepared via a conventional solid-state reaction route. X-ray Rietveld refined diffractograms of all the compositions showed the formation of an orthorhombic structure having the $Cmc2_1$ space group. Scanning electron microscopy (SEM) images revealed that the substitution of alkaline-earth metal ions promotes grain growth. Aliovalent doping of Ca^{2+}, Sr^{2+}, and Ba^{2+} enhanced the conductivity by increasing the oxygen vacancy concentration. However, among all of the studied dopants, 2% Ca^{2+}-doped Y_3GaO_6 was found to be more effective in increasing the ionic conductivity as ionic radii mismatch is minimum for Y^{3+}/Ca^{2+}. The total conductivity of 2% Ca-doped Y_3GaO_6 composition calculated using the complex impedance plot was found to be $\sim 0.14 \times 10^{-3}$ S cm^{-1} at 700 °C, which is comparable to many other reported solid electrolytes at the same temperature, making it a potential candidate for future electrolyte material for solid oxide fuel cells (SOFCs). Total electrical conductivity measurement as a function of oxygen partial pressure suggests dominating oxide-ion conduction in a wide range of oxygen partial pressure (ca. 10^{-20}−10^{-4} atm). The oxygen-ion transport is attributed to the presence of oxygen vacancies that arise from doping and conducting oxide-ion layers of one, two-, or three-dimensional channels within the crystal structure. The oxide-ion migration pathways were analyzed by the bond valence site energy (BVSE)-based approach. Photoluminescence analysis, dilatometry, Fourier transform infrared (FTIR) spectroscopy, and scanning electron microscopy studies were also performed to verify the experimental findings.

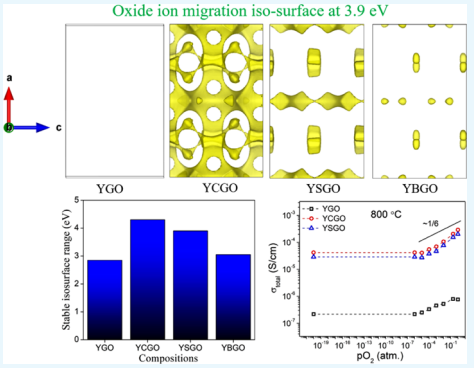

INTRODUCTION

A mismatch in the demand and supply of energy to the world's requirement compels the world to look for some alternative sources of energy, which can efficiently produce electricity. Fuel cells, especially solid oxide fuel cells (SOFCs), have received considerable attention because of its higher energy conversion efficiency.[1−3] In SOFC, a very good oxide-ion conduction is needed for its electrolyte part; besides electrolytes, oxygen-ion conductors have received considerable attention due to their wide applications in various electrochemical devices such as gas sensors, electrolyzer cells, catalysts, and separation membranes. Oxide-ion conductors are generally used as a solid electrolyte in solid oxide fuel cells.[4−6] A variety of diverse structured families such as fluorite structured,[7,8] perovskite structured,[9−12] scheelite type,[13] melilite-based structured,[14,15] apatite structured,[16,17] pyrochlore,[18,19] layered perovskite,[20−23] double perovskite,[24−26] Ruddlesden−Popper,[27−32] aurivillius phase,[33,34] brownmillerites,[35,36] hexagonal perovskite derivatives,[37−40] and $BaNdInO_4$-based oxides[35−38] are well reported and investigated for oxide-ion conduction. But still, a lot of studies are being conducted for the discovery of new families of oxide-ion conductors that may have sufficient ionic conductivity in intermediate- or lower-temperature range (300−700 °C). A recent report using first-principles calculations predicted that the Ln_3GaO_6 (Ln = La, Nd, Gd, Tb, Ho, Dy, Er, or Lu) system might be a good oxide-ion-conducting system.[44] However, earlier, a few experimental studies on some derivatives of these species have also been carried out by researchers. Purohit et al. had reported the Nd_3GaO_6-based system as a new family of oxide-ion conductor.[45] They tested Ca^{2+} and Sr^{2+} as dopants at Nd site and found an enhancement in the conductivity by more than 3 orders of magnitude. A recent study was also carried out on the synthesis and electrical properties of alkali-earth-substituted Gd_3GaO_6 oxide-ion and proton conductors,[46] and it shows a total oxide-ion conductivity at 800 °C, $\sigma_{800\ °C} = 1 \times 10^{-2}$ S cm^{-1}, for the highest substitution level of Ca^{2+}. In the

Received: July 18, 2020
Accepted: October 6, 2020
Published: November 16, 2020

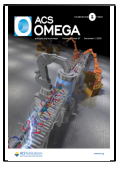

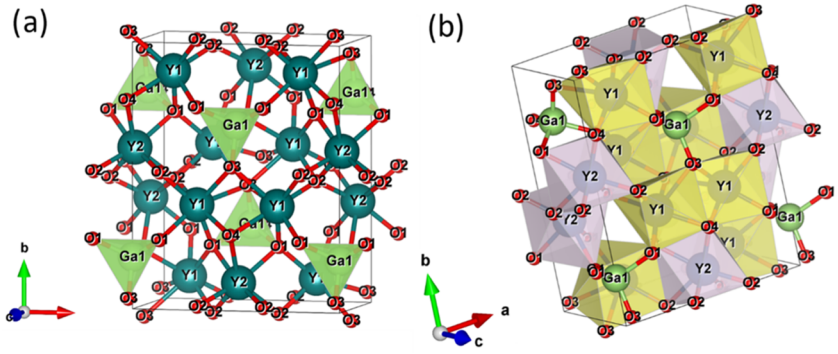

Figure 1. Crystal structure of Y_3GaO_6 with (a) GO_4 tetrahedra and (b) YO_7 pentagonal bipyramid projected in 3D. The blue, green, and red spheres represent the Y^{3+}, Ga^{3+}, and O^{2-} ions, respectively. The green polyhedra represent GO_4 tetrahedra, and the pink and yellow polyhedra represent the YO_7 pentagon.

present study, we have tried to investigate the electrochemical properties of undoped and doped Y_3GaO_6 systems, which is analogous to Gd_3GaO_6 oxide-ion and proton conductors. Till now, apart from structural studies, only a few optical studies like luminescence behavior of tri-yttrium gallate (Y_3GaO_6) are reported.[47,48] Here, we have explored the potential of doped Y_3GaO_6 as an oxide-ion-conducting material. To the best of our knowledge, this is the first study on oxide-ion conduction in alkaline-earth-metal-doped Y_3GaO_6. There are four compounds that can be formed with $Y_2O_3-Ga_2O_3$ pseudo-binary systems, viz., $YGaO_3$, $Y_3Ga_5O_{12}$, $Y_4Ga_2O_9$, and Y_3GaO_6.[49] Of these, tri-yttrium gallate (Y_3GaO_6) is a comparatively less studied system. Y_3GaO_6 crystallizes in the orthorhombic structure with space group $Cmc2_1$. This structure contains 12-Y (eight Y ions occupy 8*b*, and four Y ions occupy 4*a* Wyckoff site), 4-Ga, and 24-O atoms in a unit cell,[48] which are made up with two edge-sharing of YO_7 pentagonal bipyramids polyhedra, making a three-dimensional (3D) framework and with a GaO_4 tetrahedron. It means that the Y^{3+} cations are localized in two different asymmetrical sites of sevenfold coordination, and Ga^{3+} is in distorted oxygen tetrahedral (Figure 1).[48]

Ga^{3+} is bonded to four O^{2-} atoms to form GaO_4 tetrahedra that share a corner−corner with one YO_7 pentagonal bipyramid and an edge−edge with one YO_7 pentagonal bipyramid. Usually, the aliovalent substitution increases the oxygen vacancies to maintain the electrical neutrality of the material. Several reports are available on the enhancement of the conductivity by aliovalent substitution.[50] Here, divalent ions such as Ca^{2+}, Sr^{2+}, and Ba^{2+} are doped on the A-site (i.e., Y-site) and their effect on the bulk electrical conductivity is studied. The purpose of this study is to explore alkaline-earth-metal-doped Y_3GaO_6 as an oxide-ion-conducting material and also to identify a suitable dopant for achieving enhanced conductivity. Hereafter, the undoped Y_3GaO_6 and 2% $-Ca^{2+}$-, $-Sr^{2+}$-, and $-Ba^{2+}$-doped Y_3GaO_6 are abbreviated as YGO, YCGO, YSGO, and YBGO, respectively.

RESULTS AND DISCUSSION

Structural Analysis. Comparative X-ray diffraction (XRD) patterns of the YGO, YCGO, YSGO, and YBGO samples in the $2\theta \sim 10-120°$ region are shown in Figure 2a. All of the diffraction peaks are found to be phase-pure and indexed according to the noncentrosymmetric orthorhombic symmetry with space group $Cmc2_1$. The X-ray diffraction patterns of all of the compositions match with the standard ICSD file no. 155086. The polyhedral representation of the YGO system is shown in Figure 2b representing a similar crystal structure as earlier reported in the literature.[48] The Rietveld refinements were carried out using FullProf software taking pseudo-Voigt peak profile (Figure 3).[51] The atomic coordinates were allowed to vary free of constraints, and the values obtained in each stage were used as a starting parameter for further refinements. The occupancy factor for all of the elements was kept fixed to their nominal value. The values of lattice

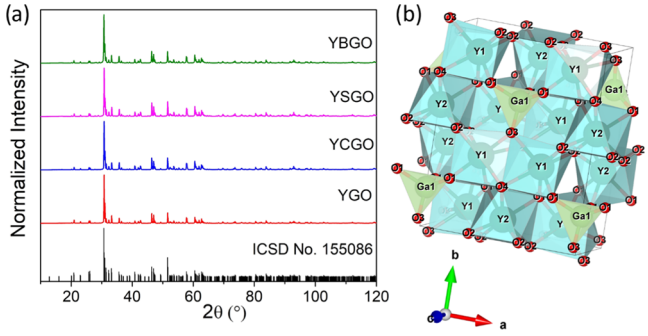

Figure 2. (a) Room-temperature XRD pattern of the studied samples and XRD pattern of Y_3GaO_6 taken from ICSD database. (b) 3D polyhedral representation of crystal structure.

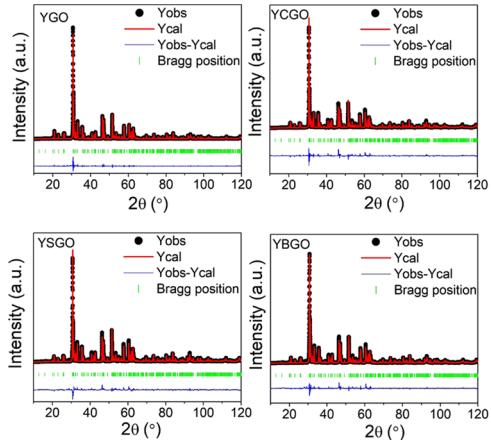

Figure 3. Rietveld refined patterns: observed (black circles), calculated (solid red line), Bragg reflections (green vertical ticks), and difference profiles (blue line) for the studied compositions sintered at 1350 °C for 6 h.

https://dx.doi.org/10.1021/acsomega.0c03433
ACS Omega 2020, 5, 30395−30404

Table 1. Rietveld Refined Lattice Parameters, Volume, Density, and Porosity of the Studied Compositions

		lattice parameters					
sample	phase	a (Å)	b (Å)	c (Å)	volume (Å^3)	relative density (%)	porosity
YGO	orthorhombic ($Cmc2_1$)	8.843(1)	11.098(1)	5.398(1)	529.765	69.98	0.300
YCGO	orthorhombic ($Cmc2_1$)	8.845(3)	11.101(6)	5.396(9)	529.970	97.61	0.024
YSGO	orthorhombic ($Cmc2_1$)	8.849(5)	11.107(1)	5.398(2)	530.599	97.61	0.024
YBGO	orthorhombic ($Cmc2_1$)	8.844(4)	11.099(6)	5.401(1)	530.226	88.40	0.116

parameters calculated from refinement are listed in Table 1. The ions Y, Ga, and O occupy 8*b*; 4*a*, 4*a*; and two 8*b* + two 4*a* Wyckoff positions, respectively. The other refinement parameters, including Wykoff positions, fractional atomic coordinates, and fitting parameters, are listed in the Supporting Information (Table S1). The coordination numbers of Y, Ga, and O atoms were found to be 7, 4, and 4, respectively, in the YGO system. After divalent doping on the Y^{3+} site, there is a slight increase in the volume as Ca^{2+} (1.20 Å), Sr^{2+} (1.35 Å), and Ba^{2+} (1.52 Å) have larger cell volume compared to Y^{3+} (1.10 Å).[52] It is easier to introduce lesser amount of Ca into the Y_3GaO_6 lattice without causing a major lattice distortion. As the doping level of Ca further increases, a secondary phase of Y_2O_3 corresponding to JCPDF no. 89−5591 is found to evolve (shown in Figure S1, Supporting Information). This indicates that the solid solubility limit of the divalent atom is only ca. 2−3%. However, for the other substituent as Sr^{2+} and Ba^{2+}, it is expected that the dissolution limit is less at the Y-site, and also, they will create much distortion in the lattice in compared to Ca^{2+} because of larger mismatch of ionic radii between the host and dopants ions.

Bond Valence Energy-Based Approach for Identification of Migration Pathways. The bond valence model is an imperative approach to evaluate the chemical credibility of inorganic crystal structures. This model is based on the bond valence sum (BVS) rule from the Pauling's electrostatic valence concept, which expresses that the sum of all bond valences linked to an atom almost equals the absolute value of its oxidation state. According to this approach, the sum of bond valences, S_{ij}, about any ion, i, is equal to its valence, V_i (i.e., the formal oxidation state)

$$V_i = \sum_j S_{ij} \tag{1}$$

where the sum runs over all adjacent atoms j of the atom i. The bond valence S_{ij} can be considered as a measure of the electrostatic flux between a cation and an anion. It is directly related to the strength of the bond and is correlated inversely with bond length. It can be estimated by the following relation

$$S_{ij} = \exp\left(\frac{R_o - R_{ij}}{B}\right) \tag{2}$$

where R_o and B are constant parameters and R_{ij} is the interatomic distance between atoms i and j. For many bonds, B is approximated to 0.37. The bond valence approach is also used to explain the structural distortions from the ideal three-dimensional crystal structure by calculating the global instability index parameter.[53,54] The energy barriers obtained by the BVS analysis are only relative to and not as accurate as the ones obtained by more sophisticated computational methods. To explore a new family of oxide-ion conductor, we examined the bond valence energy (BVE) landscapes (BVELs) of O^{2-} ions diffusion in a few yttrium-containing oxide materials.[55,56] Using the BVE approach, the BV-based energy barrier for Y_3GaO_6 was found to ∼0.54 eV along the *c*-axis of the crystal structure. Hence, due to the less energy barrier compared to other Y-containing oxide systems, this system was taken for further study. The migration pathways in the BVE calculations were constructed with linearly interpolated images between the fully relaxed starting and ending structures. The energy barrier for oxygen migration is calculated as $E_b = E_{max} - E_{min}$, where E_{max} and E_{min} are the highest and lowest energies along the migration pathway, respectively (Figure S2). Figure 4a shows the schematic bond

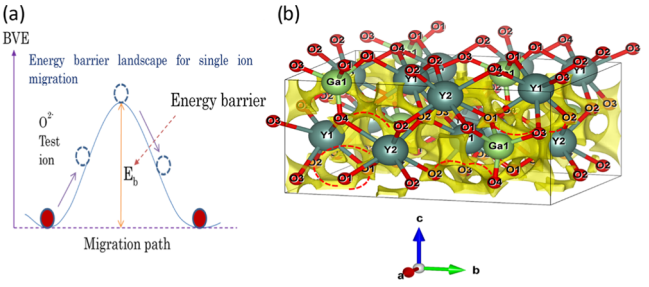

Figure 4. (a) Schematic of the energy barrier landscape of single oxide-ion migration inside the crystal lattice. (b) Crystal structure, including migration isosurface of 2.7 eV in Y_3GaO_6. The yellow color represents the isosurface. Connection of yellow isosurface represents the possible oxide-ion migration path. The dotted red lines are shown for the aid of visualization.

valence energy (BVE) landscape for the migration of single oxygen ion inside the crystal. The volumetric data in the cube file generated through SoftBV using a crystallographic information file can be directly visualized to recognize low-energy-barrier migration pathways. Moreover, through this approach, the equilibrium and interstitial sites and their connectivity through transition states can be recognized without any kind of intervention. The purpose of this approach is to identify voxels in the energy landscape, which are local minima or saddle points, and then to connect them by tracing from saddle-point voxels to minima voxels. Figure 4b shows the crystal structure and the 3D view along with the isosurface (energy value at 2.7 eV). Connection of isosurface means the existence of low-energy barrier for the oxide-ion migration and no connection on the isosurface suggests difficulty for the oxide ion to migrate across the barrier.[57−59]

Figure 5a,b shows BV-based energy landscapes for an oxide ion in YGO and YCGO at isosurface values of +2.80 and +3.90 eV, respectively, where the BV-based energy of the most stable position is set to 0 eV. The yellow isosurface of the BV-based energy of YGO did not connect across the unit cell (Figure 5b), indicating relatively difficult anion migration. On the contrary, we found that YCGO had the highest connecting pathways for oxide-ion migration across the unit cell. BV-based energy landscapes indicate that an oxide ion can migrate along

https://dx.doi.org/10.1021/acsomega.0c03433
ACS Omega 2020, 5, 30395−30404

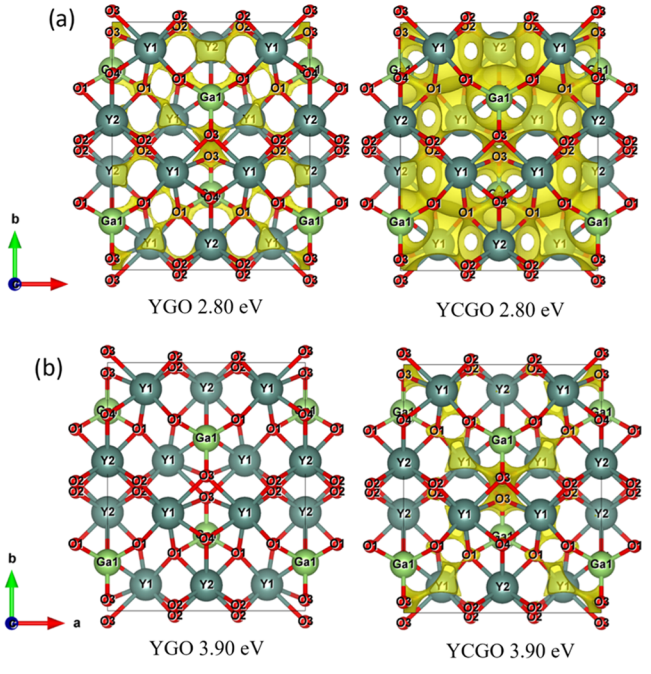

Figure 5. Oxygen-ion diffusion isosurface channel of YGO and YCGO along the *c*-axis at (a) 2.80 eV and (b) 3.90 eV derived from the bond valence energy landscape using VESTA software. At an isosurface value of 3.90 eV, the migration pathways are observed for the YCGO sample, whereas at the same value, no any connected path is observed for the YGO sample.

the edges of the GaO_4 tetrahedra and the corners of the YO_7 polyhedra. Figures 4b and 5 show that the possible oxide-ion diffusion pathways in the [010] direction are via −O3−O3−O3−O1− and through the interstitials. From the reaction coordinates pathway (see Figure S3), it is evident that YGCO has no intermediate pathway segment between −O3−O3− migrations, while other compositions have pathway segments for migration. This may be a probable cause to ease the migration of O^{2-} ions across vacant oxygen sites within the YCGO crystal structure. Though, all of the crystallographic information and studies presented here are based on room-temperature XRD studies of the compositions. The BV-based energy barriers of oxide-ion migration along visualization axes *a*, *b*, and *c* were estimated and found to be minimum along the *c* direction. Therefore, it is expected that YCGO exhibit one, two-, or three-dimensional oxide-ion diffusion and relatively easier migration than that of the other studied compositions. This can also be visualized in Figure S3 and also confirmed with Figure S4 of reaction coordinates (Supporting Information).

Conductivity Analysis. The complex impedance plot of all of the studied samples at 600 °C is shown in Figure 6a. The YGO and YBGO samples were found to exhibit a single depressed semicircular arc, whereas the YCGO and YSGO samples exhibit two semicircular arcs. No apparent electrode response is observed for any of the samples due to the frequency limit of the instrument. The centers of all of the semicircles lying below the *X*-axis show the presence of non-Debye-type relaxation behavior. The semicircular arcs are modeled with the equivalent circuit, and the contribution of each part is distinguished with the help of the corresponding circuit model. The equivalent circuit used to fit the data consists of two series R-CPE elements associated with bulk and

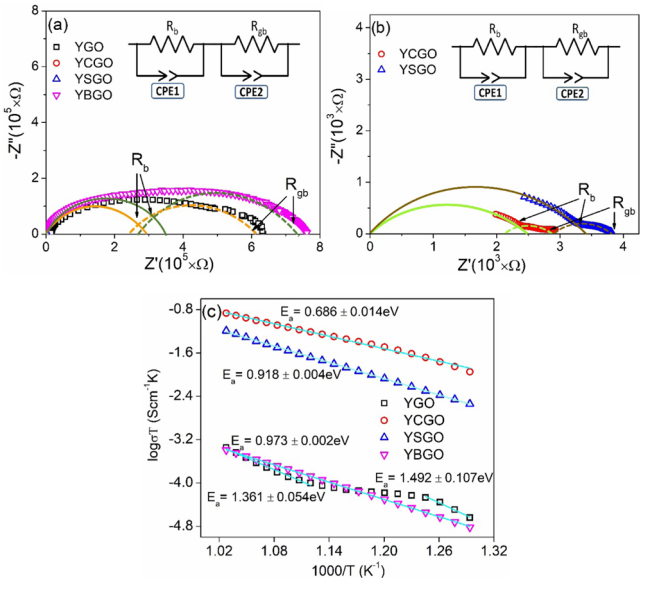

Figure 6. (a) Complex impedance plot of the studied compositions at 600 °C in air. The hollow symbol and the line represent experimental data and equivalent circuit fit, respectively. The inset represents the corresponding equivalent circuit used for fitting the impedance spectra. The solid arc in fitting represents bulk contribution, and the dotted arc represents the grain boundary contribution. (b) Complex impedance plot for the YCGO and YSGO samples. The symbol and line represent experimental data and fit, respectively. The inset represents the equivalent circuit used for fitting. (c) Arrhenius plot (variation of $\log[\sigma_{bulk}T]$ with the inverse of temperature) of the studied compositions with the inverse of temperature. The cyan line shows the linear fit, and the numbers are the calculated activation energies.

grain boundary contribution (inset of Figure 6a,b). The capacitance related to all contributions is calculated according to the following relation: $\omega = \frac{1}{RC}$, where ω is the relaxation frequency, R is the resistance, and C is indicative of bulk capacitive response. The capacitance values of bulk and grain boundary at 600 °C are listed in Table 2. The lower value of

Table 2. Value of Grain, Grain Boundary Capacitance, Total Conductivity at 600 °C, and Activation Energy of Studied Compositions

composition	C_b (F)	C_{gb} (F)	σ_{total} (S cm^{-1}) at 600 °C	activation energy (eV)
YGO	0.24×10^{-12}	0.11×10^{-9}	0.953×10^{-7}	1.361
YCGO	1.62×10^{-9}	4.14×10^{-6}	0.572×10^{-4}	0.686
YSGO	3.66×10^{-9}	8.70×10^{-6}	0.180×10^{-4}	0.918
YBGO	0.19×10^{-10}	0.29×10^{-9}	0.122×10^{-6}	0.973

constant phase element (CPE) in the higher-frequency range is the effect of bulk material, and the higher capacitance value in the lower-frequency range is because of the grain boundary contribution.

The resistances of bulk and grain boundary are calculated from the intercept of the corresponding arc on the real axis (Z'). The total resistance of the electrolyte is given by: $R_t = R_b + R_{gb}$, where R_b is the bulk resistance and R_{gb} is the grain boundary resistance. Further, this total resistance of the electrolyte was used to obtain the total conductivity using the

https://dx.doi.org/10.1021/acsomega.0c03433
ACS Omega 2020, 5, 30395−30404

formula $\sigma_t = \frac{d}{AR_t}$, where σ_t is the total conductivity, R_t is the total resistance, d is the thickness, and A is the area of the pellet. The temperature dependence of total conductivity of all of the samples is shown in Figure 6c. It is remarkable that the conductivity increases significantly for the Ca^{2+} and Sr^{2+} dopants, while it decreases for the Ba^{2+} dopant. Figure 6c depicts the Arrhenius representation of the conductivity data.[3] The activation energy (E_a) is estimated for the studied compositions using the Arrhenius equation

$$\sigma T = \sigma_0 \exp\left(\frac{-E_a}{k_B T}\right) \quad (3)$$

where σ_0 is the preexponential factor, k_B is the Boltzmann constant, and E_a is the activation energy. The activation energy has been calculated by the slope of the Arrhenius plot, which is in good agreement with a few other earlier reported prominent anionic conductors,[60−62] indicating the formation of vacancies and ionic charge carriers. The activation energy (E_a) is equal to the sum of the vacancy formation energy (E_f) and the migration barrier (E_m). The E_m value depends on the local atomic arrangement of the system. In this study, E_m, obtained from the BVE approach, is the minimum for YCGO composition among all of the doped compositions. Hence, the activation energy is minimum for the YCGO sample. The bulk conductivity of 2% Ca-doped sample (YCGO) was found to be a maximum due to the minimal mismatch of ionic radii to the host atom and the comparatively less dissociation energy in the Ca−O bond (Table S2). The highest solubility limit in $Y_{2.94}Ca_{0.06}GaO_{6-\delta}$ can be attributed to the smallest size mismatch[43] for Ca^{2+}, $|r(Ca^{2+}) - r(Y^{3+})| < |r(Sr^{2+}) - r(Y^{3+})| < |r(Ba^{2+}) - r(Y^{3+})| = 0.06 < 0.19 < 0.21$ Å. Here, r(A) denotes the ionic radius of A^{2+} cation. This leads to less activation energy of migration in the YCGO sample in comparison to others. At higher temperatures, the no. of vacancies will be dissociated; hence, the ionic conductivity is directly related to the formation of oxygen vacancies.

Effect of Dopant Size on Oxygen Partial Pressure Dependent Conductivity. For fixed valency substitution and a fixed number of vacancies, conductivity depends on the dopant size. The total conductivity variation against the ratio of dopant radii and host radii is shown in Figure 7a. The

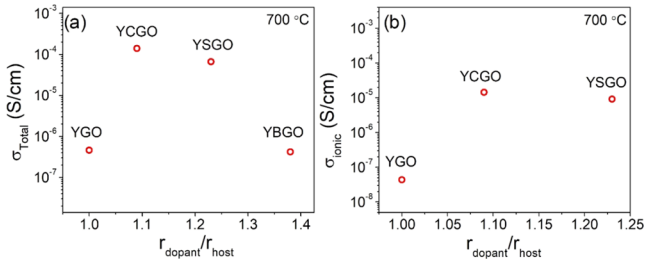

Figure 7. Dependence of (a) total conductivity and (b) oxide-ion conductivity on the dopant ionic radii at 700 °C.

maximum conductivity is obtained for Ca^{2+} doping with $r_{Ca^{2+}}/r_{Y^{3+}} \sim 1.09$. These types of optimum values are observed in many other ionic conductors such as $NdGaO_3$, $LaAlO_3$, $BaGdInO_4$, $La_{9.33}X_{0.67}Si_6O_{26}$, and $Na_{0.5}Bi_{0.5}TiO_3$.[12,17,41,63−65] It is believed that the maximum conductivity appears for $r_{dopant}/r_{host} \sim 1.05$ in the perovskite- and brownmillerite-type structure.[63]

The comparable size of dopant and host minimizes the local strain in the lattice and assists the migration of oxygen ion (shown in Supporting Information Figure S5).[63] The total conductivity as a function of oxygen partial pressure at 700 and 800 °C is shown in Figure 8. The flat region at a lower partial

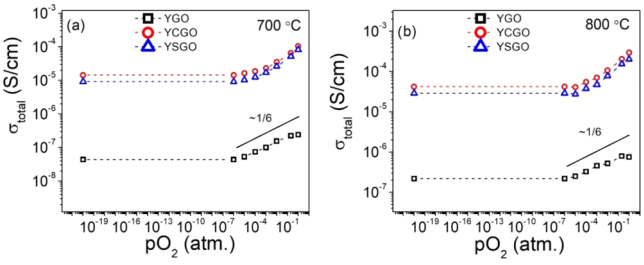

Figure 8. Oxygen partial pressure dependence of the total electrical conductivity of the YGO, YCGO, and YSGO samples at (a) 700 and (b) 800 °C, respectively. It suggests the dominant oxide-ion-type conduction in the pressure range of 10^{-4}−10^{-20} atm.

pressure in all of the studied samples is attributed to predominant ionic contribution and the positive slope of the curve at $pO_2 > 10^{-4}$ atm, showing p-type conduction with a predominant hole conductivity. The extent of ionic contribution is changing with substitution and temperature. As the hole and electron concentrations increase rapidly with the increase in temperature, the mobility of oxide ion decreases.[42] The process of hole formation can be described by the equation

$$V_O^{\bullet\bullet} + \frac{1}{2}O_2 \leftarrow O_O^X + 2h^{\bullet} \quad (4)$$

Thus, the total conductivity will be given by

$$\sigma_{total} = \sigma_p \sim V_O^{\bullet\bullet 1/2} P(O_2)^{1/6} \quad (5)$$

where $V_O^{\bullet\bullet}$ is nearly constant and the slope of $\log \sigma$ vs $\log pO_2$ is ~1/6 in the higher-partial-pressure region. In the lower-pO_2 region (<10^{-4} atm), the concentration of oxygen vacancies is higher than the concentration of holes and electron, and the total conductivity is given by

$$\sigma_{total} = \sigma_{V_O^{\bullet\bullet}} = \text{constant} \quad (6)$$

Since Y^{3+}, Ga^{3+}, Ca^{2+}, Sr^{2+}, and Ba^{2+} are neither prone to oxidation nor reduction, we can expect the conductivity to remain constant at a lower partial pressure. Further, as the mobilities of cationic species such as Y^{3+}, Ga^{3+}, Ca^{2+}, and Sr^{2+} are negligible, we can conclude that the conductivity is mainly because of oxide ions in the given range of oxygen partial pressures. The variation of ionic conductivity with dopant size at 700 °C is shown in Figure 7b.

UV−Vis Analysis. Figure 9 depicts the band gap variation of the studied composition. The band gap of the studied compositions was calculated using Tauc's relation,[66] represented by the relation:

$$\alpha h\upsilon = A(h\upsilon - E_g)^n \quad (7)$$

where A is a constant, $h\upsilon$ is the energy, α is the absorption coefficient, E_g is the band gap, and n is the probability transition rate; $n = 1/2$ for direct transition and $n = 2$ for indirect transition. The observed direct band gap of pure YGO is found to be 5.49 eV, and its value is found to decrease with the divalent doping. This decrease in band gap results in an increase in the oxygen vacancies formed by the charge

https://dx.doi.org/10.1021/acsomega.0c03433
ACS Omega 2020, 5, 30395−30404

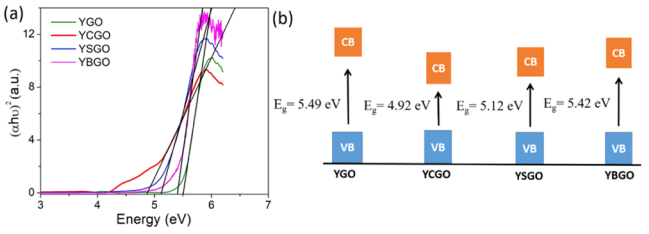

Figure 9. (a) Tauc's plot for direct band gap calculation of the YGO, YCGO, YSGO, and YBGO samples. The band gap calculated by extrapolating the fitted line to the *x*-axis and (b) the corresponding band structure.

compensation mechanism.[67] Among all of the doped compositions, Ca^{2+} has the lowest solution energy on Y^{3+} for creating oxygen defects. So, the number of defects formed will be maximum for Ca^{2+}. This type of behavior is observed in $NdBaInO_4$.[43]

Further, these results are also evident from the photoluminescence (PL) analysis (discussed in detail in the Supporting Information). The room-temperature photoluminescence spectra of the YGO, YCGO, and YSGO samples are shown in Figure S6. All of the compositions exhibit a broad and strong peak at ∼420 nm. The PL spectra could be used to describe the charge carrier trapping, transfer, and electron−hole pair interaction. The emission band located at ∼420 nm is mainly due to the formation of defects associated with the divalent dopant. The photoluminescence intensity also varies according to the surface oxygen vacancies and defects.[68] Usually, lower PL intensity corresponds to higher conductivity because of the lower recombination rate and effective charge carrier separation.[68] Its intensity is found to decrease with the dopant, with a minima for Ca doping. This suggests that the vacancy concentration is maximum for Ca doping.

Fourier Transform Infrared (FTIR) Analysis. Fourier transform infrared spectroscopy is used to get information about the chemical bond and structure of the material. The bands are formed by bending and stretching of vibrations. The FTIR spectra of the undoped and Ca^{2+}-, Sr^{2+}-, and Ba^{2+}-doped YGO samples are shown in Figure 10. The characteristic peak

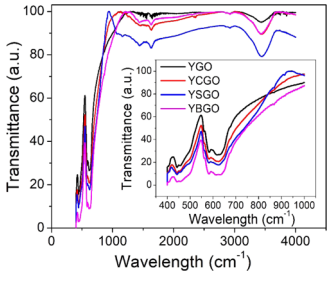

Figure 10. Room-temperature FTIR spectra of the YGO, YCGO, YSGO, and YBGO samples. The inset shows the decrease in the metal−oxygen bond intensity with an increase in the atomic mass of dopant.

around 3400 cm^{-1} is assigned to the stretching vibrations of O−H associated with the hydroxyl group.[69] The peak around 1600 cm^{-1} is attributed to the H−O−H bending vibration. As the synthesized compositions do not contain any O−H molecule-based precursor and the XRD of the samples also do not show any impure phases, we can conclude that the OH peak observed in the spectrum is because of the moisture adsorbed on the powder sample during measurements. To further confirm this, we have added the thermogravimetric analysis (TGA) measurement of YSGO in the Supporting Information (Figure S7). A strong band at 526−694 cm^{-1} is attributed to the stretching of the Y−O vibrations,[70] and the band originated at 450, and 627 cm^{-1} is assigned to Ga−O vibrations, probably due to the formation of metal oxide bond. However, a slight decrease in the magnitude and peak broadening is observed after doping with alkali-earth metal, mainly because of the increase in the defects and distortion caused by dopant ion in the host lattice.[71] The Ca−O peak around 300−400 cm^{-1} is not observed in the band. The presence of a band around 2350 cm^{-1} in the YCGO sample can be attributed to the Ca−O bond.[72] The peak around 870 cm^{-1} present in the YSGO sample is assigned to the Sr−O bond, and the kink around 860 cm^{-1} is assigned to the Ba−O bond.[73]

Scanning Electron Microscopy (SEM) Analysis. The SEM images of the fractured cross section of the YGO, YCGO, and YSGO samples are shown in Figure 11. Irregular and

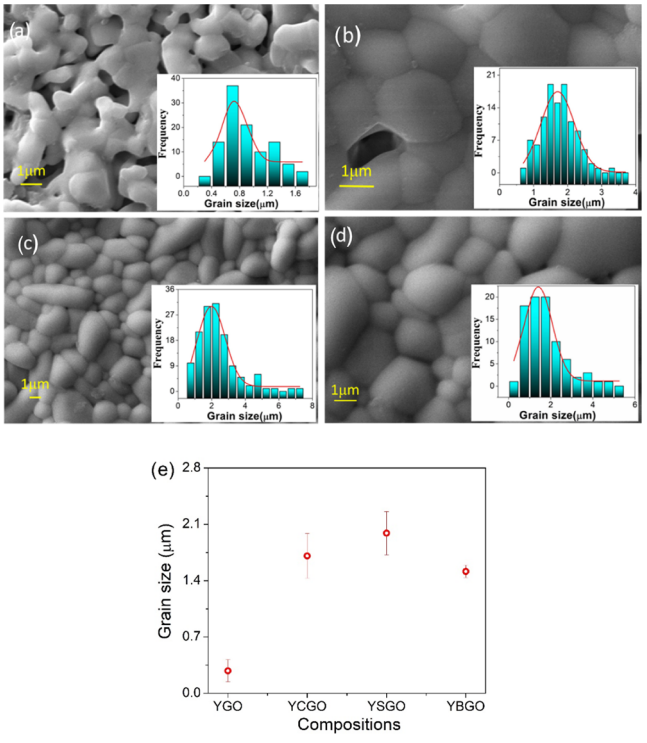

Figure 11. (a−d) SEM micrographs of the YGO, YCGO, YSGO, and YBGO samples. The insets show grain size distribution. (e) Grain size variation of the studied compositions.

agglomerated grains for the YGO sample are attributed to poor sinterability of the material. However, micrographs of the alkaline-earth-metal-doped YGO samples show quite dense and polygonal morphology with low porosity. The densification of the doped samples indicates the improvement in the sinterability after doping. Grains become more connected after doping, and the effective number of grain boundaries increases. Energy-dispersive X-ray (EDX) mapping of the YGO, YCGO, and YSGO samples (see Figure S8) confirms the presence of all of the constituent elements in the matrix. The average grain size is calculated using ImageJ software. Grain size is observed to increase with the doping of alkaline-earth metal ions. The

https://dx.doi.org/10.1021/acsomega.0c03433
ACS Omega 2020, 5, 30395−30404

density of all of the sample was calculated using the Archimedes principle. The density is found to increase with the alkaline earth doping,[17,74] as summarized in Table 1. The increase in density is correlated with the increase in grain size, as observed in the SEM micrographs of the sample.

Thermal Expansion Study. The variation of thermal expansion of pure YGO, and Ca^{2+}- and Sr^{2+}-doped YGO is shown in Figure 12. No appreciable difference is observed in

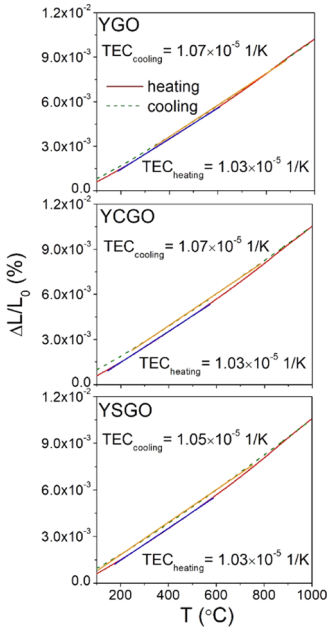

Figure 12. Thermal expansion curves of YGO, YCGO, and YSGO compositions from room temperature to 1000 °C.

the heating and cooling curves. All of the samples show a linear change with temperature. This trend also indicates the absence of any kind of structural change in the studied temperature range. Thermal expansion coefficient (TEC) can be obtained using the following relation

$$\alpha_L = \frac{\Delta L}{L \Delta T} \tag{8}$$

where α_L denotes the value of thermal expansion coefficient (TEC), L is the length of sample, ΔL is the change in length, and ΔT is the change in temperature.[75]

The TEC values of all of the samples are approximately the same. This indicates that the introduction of 2% Ca^{2+} and Sr^{2+} does not change the TEC value. Its TEC values are close to lightly doped $La_{1-x}Sr_xMnO_3$, so it will exhibit better thermal compatibility with the $LaMnO_3$ family cathode materials. The obtained TEC values (mentioned in Table 3) are also corroborated with the TEC values of many manganite- and nickelate-based cathode materials, as reported in the literature.[76]

CONCLUSIONS

Doping of a small amount of alkaline-earth metal ion has a remarkable effect on the properties of Y_3GaO_6. Partially replacing the Y by 2% Ca^{2+} or Sr^{2+} improves the bulk conductivity by more than 3 orders without any alteration in the conduction mechanism. However, the doping of Ba^{2+} did not significantly enhances the conductivity. Higher electrical conductivity with the Ca^{2+} doping is attributed to the oxygen

Table 3. TEC Values of the Measured Samples between Room Temperature and 1000 °C

compositions	thermal expansion coefficient, $\alpha_L \times 10^{-6}$ (K^{-1})
YGO	10.7
YCGO	10.7
YSGO	10.5
YBGO	–

vacancies and the formation of migration channels only. Doping of alkaline-earth metals in Y_3GaO_6 results in an increase in the conductivity and decrease in the band gap. Despite higher polarizability and lower bond strength of Sr^{2+} with O, Ca^{2+} doping was found to be more effective and efficient than Sr^{2+}. This is attributed to the optimum dopant size mismatch with the host ion as it produces minimum strain in the crystal lattice. The microstructures show an increase in grain size and densification after doping of alkaline-earth metals. This is due to the lower melting points of Ca^{2+}, Sr^{2+}, and Ba^{2+} compared to that of Y^{3+}. The bond valence energy-based approach was employed to screen and identify the oxide-ion migration pathways in the crystal structure of the investigated compositions. The oxygen partial pressure dependence of the total electrical conductivity (pO_2) study at 700 and 800 °C confirms that the material is an oxide ionic conductor in a wide range of partial pressure (ca. 10^{-20}–10^{-4} atm). Furthermore, this system has the potential to improve its ionic conductivity on further optimizing dopant and synthesis method. The other structural, microstructural (SEM), thermal (TEC, TGA), and optical characterizations (PL, UV, FTIR) also support the XRD, BVE, and electrical behavior and are correlated with the experimental findings. Thus, this study explores a new family of anionic conductors that in the future may be used in electrochemical device applications.

EXPERIMENTAL SECTION

Sample Preparation. Polycrystalline samples of Y_3GaO_6 and 2% Ca^{2+}-, Sr^{2+}-, and Ba^{2+}-doped-Y_3GaO_6 were prepared via the solid-state reaction route. The Y_2O_3 (Otto, 99.99%), $CaCO_3$ (Alfa Aesar, 99.5%), $SrCO_3$ (Loba Chemie, 99.9%), $BaCO_3$ (Alfa Aesar, 99.9%), and Ga_2O_3 (Alfa Aesar, 99.99%) were preheated at 300 °C for 5 h and weighed in a stoichiometric amount. The raw powders were then mixed in a mortar thoroughly using acetone as a mixing media. After grinding, the powder was calcined at 900 °C for 12 h in air. Then, the calcined powders were mixed with 2% poly(vinyl alcohol) and uniaxially pressed into pellets by applying a load of $\sim 6 \times 10^{-5}$ MPa. The samples were then sintered at 1200 °C for 24 h and at 1350 °C for 6 h in air.

Characterizations. The structural study was done by a Rigaku Miniflex-II desktop X-ray diffractometer with Cu Kα_1 radiation in the 2θ range of 10–120° and at a scan rate of 5° min^{-1}. The bulk density was calculated using the Archimedes density measurement kit (DENVER SI-234). Surface morphology and composition analysis of polished samples were carried out using SEM (EVO-scanning electron microscope MA15/18). Impedance measurement was carried out on a sintered pellet in an ambient atmosphere via a Wayne Kerr 6500P series LCR meter using a two-probe method. Data were collected in the temperature range of 400–700 °C using platinum paste as the electrode. The total conductivity as a function of oxygen partial pressure was measured by a conventional DC-2W method using a Keysight 34970A precise digital multimeter

https://dx.doi.org/10.1021/acsomega.0c03433
ACS Omega 2020, 5, 30395–30404

with data acquisition mode. The measurements were done in a temperature range of 650−800 °C. To introduce the proper atmosphere to the measurement cell, a gas mixer was used. The atmospheres were changed from pure and dry argon to dry oxygen, and the step was 0.1 atm. During the measurements, the samples were held at the final temperature to see the constant value of recorded resistance, which indicated the thermodynamic equilibrium between the sample and gas. This procedure was repeated in every temperature and atmosphere. UV−visible absorption spectra in the wavelength range of 200−1000 nm were recorded using a JASCO V-770 UV−vis spectrometer. Room-temperature photoluminescence measurement was done using a photoluminescence spectrometer (Fluorolog Horiba Scientific) employing an excitation wavelength of 260 nm. Fourier transform infrared spectra were recorded using a Nicolet iS5 THERMO Electron Scientific Instruments LLC in the wavenumber range of 400−4000 cm^{-1} using KBr media. Thermogravimetric analysis of the sample was done in a nitrogen atmosphere using a Netzsch Jupiter449 F1 (Burlington, MA) with a gas flow rate of 100 mL min^{-1}. Thermal expansion of bulk sample in the temperature range of 50−1000 °C was studied using a Netzsch DIL 420 PC/4 dilatometer with a constant cooling and heating rate of 2 °C min^{-1} in airflow. The thermal expansion coefficient is calculated by linear fitting the elongation vs temperature function.

Bond Valence Energy Calculations. To inspect the oxide-ion diffusion path and migration barrier in the crystal structure, we have done bond valence-based energy calculations using SoftBV program.[56] The room-temperature X-ray Rietveld refined crystallographic information file parameters were used for the bond valence energy calculations, and the BVE landscape and crystal structure were drawn using Vesta software.[77] The spatial resolution in the calculation was set to 0.1 Å. The energy barriers for oxide-ion migration were estimated using the BVE landscape.

■ ASSOCIATED CONTENT

Supporting Information

The Supporting Information is available free of charge at https://pubs.acs.org/doi/10.1021/acsomega.0c03433.

X-ray diffractograms of the Ca-doped-YGO samples at room temperature, bond valence energy landscape for oxide-ion migration viewed along the *c* axis with various isosurfaces and energy barrier histogram, oxygen-ion diffusion migration pathways, BVEL showing migration along the faces and edges of the GO_4 tetrahedra and the YO_7 pentagonal bipyramid, Rietveld refinement parameters, intrinsic strain calculated using the Williamson−Hall analysis, bonding strength with the oxygen of divalent A-site dopant, room-temperature photoluminescence analysis, thermogravimetric analysis of the YSGO sample, and EDX mapping (PDF)

■ AUTHOR INFORMATION

Corresponding Authors

Raghvendra Pandey − *Department of Physics, A.R.S.D. College, University of Delhi, New Delhi 110021, India;* orcid.org/0000-0002-7061-0352; Email: raghvendra@arsd.du.ac.in

Prabhakar Singh − *Department of Physics, Indian Institute of Technology (Banaras Hindu University), Varanasi 221005, India;* orcid.org/0000-0001-5104-0131; Email: psingh.app@iitbhu.ac.in

Authors

Pragati Singh − *Department of Physics, Indian Institute of Technology (Banaras Hindu University), Varanasi 221005, India*

Tadeusz Miruszewski − *Faculty of Applied Physics and Mathematics, and Advanced Materials Centre, Gdansk University of Technology, 80-233 Gdansk, Poland*

Kacper Dzierzgowski − *Faculty of Applied Physics and Mathematics, and Advanced Materials Centre, Gdansk University of Technology, 80-233 Gdansk, Poland*

Aleksandra Mielewczyk-Gryn − *Faculty of Applied Physics and Mathematics, and Advanced Materials Centre, Gdansk University of Technology, 80-233 Gdansk, Poland;* orcid.org/0000-0001-6795-3840

Complete contact information is available at: https://pubs.acs.org/10.1021/acsomega.0c03433

Notes

The authors declare no competing financial interest.

■ ACKNOWLEDGMENTS

This work was partially supported by the DST-SERB through the project grant no. CRG/2018/001926. R.P. acknowledges the support of DST-SERB for the ECRA project (ECR/2016/001152).

■ REFERENCES

(1) Ormerod, R. M. Solid Oxide Fuel Cells. *Chem. Soc. Rev.* **2003**, *32*, 17−28.

(2) McCombie, K. S.; Wildman, E. J.; Fop, S.; Smith, R. I.; Skakle, J. M. S.; McLaughlin, A. C. The Crystal Structure and Electrical Properties of the Oxide Ion Conductor $Ba_3WNbO_{8.5}$. *J. Mater. Chem. A* **2018**, *6*, 5290−5295.

(3) Raghvendra; Singh, R. K.; Singh, P. Electrical Conductivity of Barium Substituted LSGM Electrolyte Materials for IT-SOFC. *Solid State Ionics* **2014**, *262*, 428−432.

(4) Goodenough, J. B. Ceramic Technology: Oxide-Ion Conductors by Design. *Nature* **2000**, *404*, 821−823.

(5) Skinner, S. J.; Kilner, J. A. Oxygen Ion Conductors. *Mater. Today* **2003**, *6*, 30−37.

(6) Malavasi, L.; Fisher, C. A. J.; Islam, M. S. Oxide-Ion and Proton Conducting Electrolyte Materials for Clean Energy Applications: Structural and Mechanistic Features. *Chem. Soc. Rev.* **2010**, *39*, 4370−4387.

(7) Boivin, J. C.; Mairesse, G. Recent Material Developments in Fast Oxide Ion Conductors. *Chem. Mater.* **1998**, *10*, 2870−2888.

(8) Yashima, M. Invited Review: Some Recent Developments in the Atomic-Scale Characterization of Structural and Transport Properties of Ceria-Based Catalysts and Ionic Conductors. *Catal. Today* **2015**, *253*, 3−19.

(9) Ishihara, T.; Matsuda, H.; Takita, Y. Doped $LaGaO_3$ Perovskite Type Oxide as a New Oxide Ionic Conductor. *J. Am. Chem. Soc.* **1994**, *116*, 3801−3803.

(10) Sinha, A.; Sharma, B. P.; Gopalan, P. Development of novel perovskite based oxide ion conductor. *Electrochim. Acta* **2006**, *51*, 1184−1193.

(11) Li, M.; Pietrowski, M. J.; De Souza, R. A.; Zhang, H.; Reaney, I. M.; Cook, S. N.; Kilner, J. A.; Sinclair, D. C. A Family of Oxide Ion Conductors Based on the Ferroelectric Perovskite Na0.5Bi0.5TiO3. *Nat. Mater.* **2014**, *13*, 31−35.

(12) Ishihara, T.; Matsuda, H.; bin Bustam, M. A.; Takita, Y. Oxide Ion Conductivity in Doped Ga Based Perovskite Type Oxide. *Solid State Ionics* **1996**, *86*−*88*, 197−201.

(13) Takai, S.; Sugiura, K.; Esaka, T. Ionic Conduction Properties of $Pb_{1-x}M_xWO_{4+\delta}$ (M = Pr, Tb). *Mater. Res. Bull.* **1999**, *34*, 193−202.
(14) Kuang, X.; Green, M. A.; Niu, H.; Zajdel, P.; Dickinson, C.; Claridge, J. B.; Jantsky, L.; Rosseinsky, M. J. Interstitial Oxide Ion Conductivity in the Layered Tetrahedral Network Melilite Structure. *Nat. Mater.* **2008**, *7*, 498−504.
(15) Rozumek, M.; Majewski, P.; Sauter, L.; Aldinger, F. $La_{1+x}Sr_{1-x}Ga_3O_{7-\delta}$ Melilite-Type Ceramics: Preparation, Composition, and Structure. *J. Am. Ceram. Soc.* **2004**, *87*, 662−669.
(16) Ma, Y.; Moliere, M.; Yu, Z.; Fenineche, N.; Elkedim, O. Novel Chemical Reaction Co-Precipitation Method for the Synthesis of Apatite-Type Lanthanum Silicate as an Electrolyte in SOFC. *J. Alloys Compd.* **2017**, *723*, 418−424.
(17) Beaudet-Savignat, S.; Vincent, A.; Lambert, S.; Gervais, F. Oxide Ion Conduction in Ba, Ca and Sr Doped Apatite-Type Lanthanum Silicates. *J. Mater. Chem.* **2007**, *17*, 2078−2087.
(18) Van Dijk, M. P.; de Vries, K. J.; Burggraaf, A. J. Oxygen Ion and Mixed Conductivity in Compounds. *Solid State Ionics* **1983**, *9 & 10*, 913−920.
(19) Uno, W.; Fujii, K.; Niwa, E.; Torii, S.; Miao, P.; Kamiyama, T.; Yashima, M. Experimental Visualization of Oxide-Ion Diffusion Paths in Pyrochlore-Type $Yb_2Ti_2O_7$. *J. Ceram. Soc. Jpn.* **2018**, *126*, 341−345.
(20) Lee, C. K.; West, A. R. Thermal Behaviour and Polymorphism of BIMEVOX Oxide Ion Conductors Including the New Materials: $Bi_4V_2O_{11}$: M; M = La, Y, Mg, B. *Solid State Ionics* **1996**, *86−88*, 235−239.
(21) Pirovano, C.; Steil, M. C.; Capoen, E.; Nowogrocki, G.; Vannier, R. N. Impedance Study of the Microstructure Dependence of the Electrical Properties of BIMEVOXes. *Solid State Ionics* **2005**, *176*, 2079−2083.
(22) Iharada, T.; Hammouche, A.; Fouletier, J.; Kleitz, M.; Boivin, J. C.; Mairesse, G. Electrochemical Characterization of BIMEVOX Oxide-Ion Conductors. *Solid State Ionics* **1991**, *48*, 257−265.
(23) Abraham, F.; Boivin, J. C.; Mairesse, G.; Nowogrocki, G. The Bimevox Series: A New Family of High Performances Oxide Ion Conductors. *Solid State Ionics* **1990**, *40−41*, 934−937.
(24) Burriel, M.; Peña-Martínez, J.; Chater, R. J.; Fearn, S.; Berenov, A. V.; Skinner, S. J.; Kilner, J. A. Anisotropic Oxygen Ion Diffusion in Layered $PrBaCo_2O_{5+\delta}$. *Chem. Mater.* **2012**, *24*, 613−621.
(25) Yashima, M. Disorder and Diffusion Path of Oxide Ions in Ion Conductors. *Nihon Kessho Gakkaishi* **2004**, *46*, 232−237.
(26) Sengodan, S.; Choi, S.; Jun, A.; Shin, T. H.; Ju, Y. W.; Jeong, H. Y.; Shin, J.; Irvine, J. T. S.; Kim, G. Layered Oxygen-Deficient Double Perovskite as an Efficient and Stable Anode for Direct Hydrocarbon Solid Oxide Fuel Cells. *Nat. Mater.* **2015**, *14*, 205−209.
(27) Yashima, M.; Sirikanda, N.; Ishihara, T. Crystal Structure, Diffusion Path, and Oxygen Permeability of a Pr_2NiO4-Based Mixed Conductor (Pr0.9la 0.1)2(Ni0.74Cu0.21Ga 0.05)$O_{4+\delta}$. *J. Am. Chem. Soc.* **2010**, *132*, 2385−2392.
(28) Ishihara, T.; Nakashima, K.; Okada, S.; Enoki, M.; Matsumoto, H. Defect Chemistry and Oxygen Permeation Property of $Pr_2Ni_{0.75}Cu_{0.25}O_4$ Oxide Doped with Ga. *Solid State Ionics* **2008**, *179*, 1367−1371.
(29) Yamada, A.; Suzuki, Y.; Saka, K.; Uehara, M.; Mori, D.; Kanno, R.; Kiguchi, T.; Mauvy, F.; Grenier, J. C. Ruddlesden-Popper-Type Epitaxial Film as Oxygen Electrode for Solid-Oxide Fuel Cells. *Adv. Mater.* **2008**, *20*, 4124−4128.
(30) Amow, G.; Skinner, S. J. Recent Developments in Ruddlesden-Popper Nickelate Systems for Solid Oxide Fuel Cell Cathodes. *J. Solid State Electrochem.* **2006**, *10*, 538−546.
(31) Patrakeev, M. V.; Leonidov, I. A.; Kozhevnikov, V. L.; Kharton, V. V. Ion-Electron Transport in Strontium Ferrites: Relationships with Structural Features and Stability. *Solid State Sci.* **2004**, *6*, 907−913.
(32) Yashima, M.; Enoki, M.; Wakita, T.; Ali, R.; Matsushita, Y.; Izumi, F.; Ishihara, T. Structural Disorder and Diffusional Pathway of Oxide Ions in a Doped Pr_2NiO_4-Based Mixed Conductor. *J. Am. Chem. Soc.* **2008**, *130*, 2762−2763.
(33) Kendall, K. R.; Navas, C.; Thomas, J. K.; Zur Loye, H. C. Recent Developments in Oxide Ion Conductors: Aurivillius Phases. *Chem. Mater.* **1996**, *8*, 642−649.
(34) Thomas, J. K.; Anderson, E. M.; Krause, W. E.; Loye, H. Z. Oxygen Ion Conductivity in a New Class of Layered Bismuth Oxide Compounds. *MRS Proc.* **1992**, *293*, 295−300.
(35) Auckett, J. E.; Studer, A. J.; Pellegrini, E.; Ollivier, J.; Johnson, M. R.; Schober, H.; Miiller, W.; Ling, C. D. Combined Experimental and Computational Study of Oxide Ion Conduction Dynamics in $Sr_2Fe_2O_5$ Brownmillerite. *Chem. Mater.* **2013**, *25*, 3080−3087.
(36) Goodenough, J. B.; Ruiz-Diaz, J. E.; Zhen, Y. S. Oxide-Ion Conduction in $Ba_2In_2O_5$ and $Ba_3In_2MO_8$ (M=Ce, Hf, or Zr). *Solid State Ionics* **1990**, *44*, 21−31.
(37) Fop, S.; Skakle, J. M. S.; McLaughlin, A. C.; Connor, P. A.; Irvine, J. T. S.; Smith, R. I.; Wildman, E. J. Oxide Ion Conductivity in the Hexagonal Perovskite Derivative $Ba_3MoNbO_{8.5}$. *J. Am. Chem. Soc.* **2016**, *138*, 16764−16769.
(38) Yashima, M.; Tsujiguchi, T.; Fujii, K.; Niwa, E.; Nishioka, S.; Hester, J. R.; Maeda, K. Direct Evidence for Two-Dimensional Oxide-Ion Diffusion in the Hexagonal Perovskite-Related Oxide $Ba_3MoNbO_{8.5-\delta}$. *J. Mater. Chem. A* **2019**, *7*, 13910−13916.
(39) Fop, S.; McCombie, K. S.; Wildman, E. J.; Skakle, J. M. S.; Mclaughlin, A. C. Hexagonal Perovskite Derivatives: A New Direction in the Design of Oxide Ion Conducting Materials. *Chem. Commun.* **2019**, *55*, 2127−2137.
(40) Fujii, K.; Shiraiwa, M.; Esaki, Y.; Yashima, M.; Kim, S. J.; Lee, S. Improved Oxide-Ion Conductivity of $NdBaInO_4$ by Sr Doping. *J. Mater. Chem. A* **2015**, *3*, 11985−11990.
(41) Yaguchi, H.; Fujii, K.; Yashima, M. A New Structure Family of Oxide-Ion Conductors Based on $BaGdInO_4$. *J. Mater. Chem. A* **2020**, *8*, 8638−8647.
(42) Fujii, K.; Esaki, Y.; Omoto, K.; Yashima, M.; Hoshikawa, A.; Ishigaki, T.; Hester, J. R. New Perovskite-Related Structure Family of Oxide-Ion Conducting Materials $NdBaInO_4$. *Chem. Mater.* **2014**, *26*, 2488−2491.
(43) Yang, X.; Liu, S.; Lu, F.; Xu, J.; Kuang, X. Acceptor Doping and Oxygen Vacancy Migration in Layered Perovskite $NdBaInO_4$-Based Mixed Conductors. *J. Phys. Chem. C* **2016**, *120*, 6416−6426.
(44) Lee, J.; Ohba, N.; Asahi, R. First-Principles Prediction of High Oxygen-Ion Conductivity in Trilanthanide Gallates Ln_3GaO_6. *Sci. Technol. Adv. Mater.* **2019**, *20*, 144−159.
(45) Purohit, R. D.; Chesnaud, A.; Lachgar, A.; Joubert, O.; Caldes, M. T.; Piffard, Y.; Brohan, L. Development of New Oxygen Ion Conductors Based on Nd_4GeO_8 and Nd3GaO6. *Chem. Mater.* **2005**, *17*, 4479−4485.
(46) Iakovleva, A.; Chesnaud, A.; Animitsa, I.; Dezanneau, G. Insight into the Synthesis and Electrical Properties of Alkali-Earth-Substituted Gd_3GaO_6 Oxide-Ion and Proton Conductors. *Int. J. Hydrogen Energy* **2016**, *41*, 14941−14951.
(47) Liu, F. S.; Liu, Q. L.; Liang, J. K.; Luo, J.; Yang, L. T.; Song, G. B.; Zhang, Y.; Wang, L. X.; Yao, J. N.; Rao, G. H. Optical Spectra of Ln3+ (Nd^{3+}, Sm^{3+}, Dy^{3+}, Ho^{3+}, Er^{3+}) Doped Y_3GaO_6. *J. Lumin.* **2006**, *111*, 278−283.
(48) Liu, F. S.; Liu, Q. L.; Liang, J. K.; Luo, J.; Yang, L. T.; Song, G. B.; Zhang, Y.; Wang, L. X.; Yao, J. N.; Rao, G. H. Crystal Structure and Photoluminescence of Tb^{3+} Doped Y3GaO6. *J. Alloys Compd.* **2006**, *425*, 278−283.
(49) Popova, V. F.; Petrosyan, A. G.; Tugova, E. A.; Romanov, D. P.; Gusarov, V. V. Y2O3-Ga2O3 Phase Diagram. *Russ. J. Inorg. Chem.* **2009**, *54*, 624−629.
(50) Verma, O. N.; Jha, P. A.; Singh, P.; Jha, P. K.; Singh, P. Influence of Iso-Valent 'Sm' Double Substitution on the Ionic Conductivity of La0.9Sr0.1Al0.9Mg0.1O3-δ Ceramic System. *Mater. Chem. Phys.* **2020**, *241*, No. 122345.
(51) Mccusker, L. B.; Von Dreele, R. B.; Cox, D. E.; Louër, D.; Scardi, P. Rietveld Refinement Guidelines. *J. Appl. Crystallogr.* **1999**, *32*, 36−50.

https://dx.doi.org/10.1021/acsomega.0c03433
ACS Omega 2020, 5, 30395−30404

(52) Shannon, R. D. Revised Effective Ionic Radii and Systematic Studies of Interatomic Distances in Halides and Chalcogenides. *Acta Crystallogr., Sect. A* **1976**, *32*, 751−767.
(53) Brese, N. E.; O'Keeffe, M. Bond-valence Parameters for Solids. *Acta Crystallogr., Sect. B: Struct. Sci.* **1991**, *47*, 192−197.
(54) Chen, H.; Wong, L. L.; Adams, S. SoftBV− a Software Tool for Screening the Materials Genome of Inorganic Fast Ion Conductors. *Acta Crystallogr., Sect. B: Struct. Sci., Cryst. Eng. Mater.* **2019**, *75*, 18−33.
(55) Adams, S. From Bond Valence Maps to Energy Landscapes for Mobile Ions in Ion-Conducting Solids. *Solid State Ionics* **2006**, *177* (), 1625−1630. DOI: 10.1016/j.ssi.2006.03.054.
(56) Adams, S. Energy Landscapes for Mobile Ions in Ion Conducting Solids. *Bull. Mater. Sci.* **2006**, *29*, 587−593.
(57) Yasui, Y.; Niwa, E.; Matsui, M.; Fujii, K.; Yashima, M. Discovery of a Rare-Earth-Free Oxide-Ion Conductor $Ca_3Ga_4O_9$ by Screening through Bond Valence-Based Energy Calculations, Synthesis, and Characterization of Structural and Transport Properties. *Inorg. Chem.* **2019**, *58*, 9460−9468.
(58) Niwa, E.; Yashima, M. Discovery of Oxide-Ion Conductors with a New Crystal Structure, $BaSc_{2-x}A_xSi_3O_{10-x/2}$ (A = Mg, Ca) by Screening Sc-Containing Oxides through the Bond-Valence Method and Experiments. *ACS Appl. Energy Mater.* **2018**, *1*, 4009−4015.
(59) Joncher, A. K. *Dielectric Relaxation in Solids*; Chelsea Dielectrics Press, 1983.
(60) Wang, X. P.; Fang, Q. F. Effects of Ca Doping on the Oxygen Ion Diffusion and Phase Transition in Oxide Ion Conductor $La_2Mo_2O_9$. *Solid State Ionics* **2002**, *146*, 185−193.
(61) Sinha, A.; Sharma, B. P.; Gopalan, P. Development of Novel Perovskite Based Oxide Ion Conductor. *Electrochim. Acta* **2006**, *51*, 1184−1193.
(62) Hung, I. M.; Peng, H. W.; Zheng, S. L.; Lin, C. P.; Wu, J. S. Phase Stability and Conductivity of $Ba_{1-y}Sr_yCe_{1-x}Y_xO_{3-\delta}$ Solid Oxide Fuel Cell Electrolyte. *J. Power Sources* **2009**, *193*, 155−159.
(63) Hayashi, H.; Inaba, H.; Matsuyama, M.; Lan, N. G.; Dokiya, M.; Tagawa, H. Structural Consideration on the Ionic Conductivity of Perovskite-Type Oxides. *Solid State Ionics* **1999**, *122*, 1−15.
(64) Kilner, J. A.; Barrow, P.; Brook, R. J.; Norgett, M. J. Electrolytes for the High Temperature Fuel Cell; Experimental and Theoretical Studies of the Perovskite $LaAlO_3$. *J. Power Sources* **1978**, *3*, 67−80.
(65) Huang, P.; Petric, A. Superior Oxygen Ion Conductivity of Lanthanum Gallate. *J. Electrochem. Soc.* **1996**, *143*, 1644−1648.
(66) Redinger, A.; Siebentritt, S. Loss Mechanisms in Kesterite Solar Cells. *Copper Zinc Tin Sulfide-Based Thin-Film Solar Cells*; John Wiley & Sons, Ltd., 2015; Vol. *627*, pp 363−386.
(67) Abdissa, Y.; Siraj, K.; Selale, G. Effect of Mg2+, Ca2+ and Sr2+ Ions Doping on the Band Gap Energy of ZnO Nanoparticle. *JOJ Mater. Sci.* **2018**, *3*, 4−9.
(68) Bhabu, K. A.; Theerthagiri, J.; Madhavan, J.; Balu, T.; Muralidharan, G.; Rajasekaran, T. R. Enhanced Electrochemical Behavior of Ceria Based Zirconia Electrolytes for Intermediate Temperature Solid Oxide Fuel Cell Applications. *J. Mater. Sci. Mater. Electron.* **2016**, *27*, 10980−10992.
(69) Bhabu, K. A.; Theerthagiri, J.; Madhavan, J.; et al. Cubic Fluorite Phase of Samarium Doped Cerium Oxide (CeO2)-0.96Sm0.04 for solid oxide fuel cell electrolyte. *J. Mater. Sci.: Mater. Electron.* **2016**, 1566−1573.
(70) Traina, C. A.; Schwartz, J. Surface Modification of Y_2O_3 Nanoparticles. *Langmuir* **2007**, *23*, 9158−9161.
(71) Manning, T. D.; Parkin, I. P.; Pemble, M. E.; Sheel, D.; Vernardou, D. Intelligent Window Coatings: Atmospheric Pressure Chemical Vapor Deposition of Tungsten-Doped Vanadium Dioxide. *Chem. Mater.* **2004**, *16*, 744−749.
(72) Gill, J. K.; Pandey, O. P.; Singh, K. Ionic Conductivity, Structural and Thermal Properties of Ca^{2+} Doped $Y_2Ti_2O_7$ Pyrochlores for SOFC. *Int. J. Hydrogen Energy* **2012**, *37*, 3857−3864.
(73) Singh, D.; Sheoran, S.; Tanwar, V.; Bhagwan, S. Optical Characteristics of Eu(III) Doped MSiO3 (M = Mg, Ca, Sr and Ba) Nanomaterials for White Light Emitting Applications. *J. Mater. Sci. Mater. Electron.* **2017**, *28*, 3243−3253.
(74) Ali, A.; Raza, R.; Kaleem Ullah, M.; Rafique, A.; Wang, B.; Zhu, B. Alkaline Earth Metal and Samarium Co-Doped Ceria as Efficient Electrolytes. *Appl. Phys. Lett.* **2018**, *112*, No. 043902.
(75) Kumar, P.; Singh, N. K.; Singh, R. K.; Singh, P. Influence of Ni/Mo Ratio on Structural and Electrical Properties of Double Perovskite System Sr2Ni1+xMo1−xO6−δ. *Appl. Phys. A: Mater. Sci. Process.* **2015**, *121*, 635−644.
(76) Sun, C.; Hui, R.; Roller, J. Cathode Materials for Solid Oxide Fuel Cells: A Review. *J. Solid State Electrochem.* **2010**, *14*, 1125−1144.
(77) Momma, K.; Izumi, F. VESTA 3 for Three-Dimensional Visualization of Crystal, Volumetric and Morphology Data. *J. Appl. Crystallogr.* **2011**, *44*, 1272−1276.

https://dx.doi.org/10.1021/acsomega.0c03433
ACS Omega 2020, 5, 30395−30404